ADVANCED MATERIALS
www.advmat.de

Designing the Bending Stiffness of 2D Material Heterostructures

Jaehyung Yu, Edmund Han, M. Abir Hossain, Kenji Watanabe, Takashi Taniguchi, Elif Ertekin, Arend M. van der Zande, and Pinshane Y. Huang**

2D monolayers represent some of the most deformable inorganic materials, with bending stiffnesses approaching those of lipid bilayers. Achieving 2D heterostructures with similar properties would enable a new class of deformable devices orders of magnitude softer than conventional thin-film electronics. Here, by systematically introducing low-friction twisted or heterointerfaces, interfacial engineering is leveraged to tailor the bending stiffness of 2D heterostructures over several hundred percent. A bending model is developed and experimentally validated to predict and design the deformability of 2D heterostructures and how it evolves with the composition of the stack, the atomic arrangements at the interfaces, and the geometry of the structure. Notably, when each atomic layer is separated by heterointerfaces, the total bending stiffness reaches a theoretical minimum, equal to the sum of the constituent layers regardless of scale of deformation—lending the extreme deformability of 2D monolayers to device-compatible multilayers.

1. Introduction

Across materials systems, interfaces represent opportunities to manipulate or realize new properties. 2D materials represent the ultimate limit for interfacial engineering, where it is possible to independently control and design each interface by stacking individual atomic layers of one or more materials held together by weak van der Waals forces.[1] The resulting structures can include aligned or twisted stacks of the same material or vertical heterostructures of different materials,[2] where one can readily alter the relative lattice constant and in-plane rotation between layers. Control over the interlayer interactions has produced remarkable electronic properties in 2D multilayers, such as emergent quantum states[3–5] and the ability to modify their bandstructure and interlayer conductivity.[6–10] Interfacial interactions are just as important to the mechanics of 2D multilayers and heterostructures, where they govern dislocation creation and propagation, interfacial friction, and bending.[11–19] In particular, 2D multilayers have been shown to exhibit unusual, interface-dominated bending properties because of their highly anisotropic structure and weak van der Waals bonds.[18,19]

2. Overview

Here, we harness interfacial engineering to demonstrate control over the bending stiffness and deformability of 2D heterostructures. We experimentally and computationally measure the bending stiffness of 2D multilayers and heterostructures while systematically engineering commensurate, twisted or heterointerfaces by varying the ordering of the layers. We build a simple model, adapted from continuum laminated and Timoshenko beam theories, to predict and design the bending stiffness of arbitrary 2D heterostructures. In this model, the complex mechanics of 2D heterostructures are reduced to two simple, measurable components: a contribution from each atomic layer and a contribution from each interface. Using this model, we show that incorporating interlayer twist and heterointerfaces reduces the interfacial friction nearly to zero. By controlling the number and position of such interfaces, we

Dr. J. Yu,[+] M. A. Hossain, Prof. E. Ertekin, Prof. A. M. van der Zande
Department of Mechanical Science and Engineering
University of Illinois at Urbana-Champaign
Urbana, IL 61801, USA
E-mail: arendv@illinois.edu

E. Han, Prof. P. Y. Huang
Department of Materials Science and Engineering
University of Illinois at Urbana-Champaign
Urbana, IL 61801, USA
E-mail: pyhuang@illinois.edu

The ORCID identification number(s) for the author(s) of this article can be found under https://doi.org/10.1002/adma.202007269.

[+]Present address: Department of Chemistry University of Chicago
Chicago, IL 60615, USA

K. Watanabe
Research Center for Functional Materials
National Institute for Materials Science
1-1 Namiki, Tsukuba, Ibaraki 305-0044, Japan

T. Taniguchi
International Center for Materials Nanoarchitectonics
National Institute for Materials Science
1-1 Namiki, Tsukuba, Ibaraki 305-0044, Japan

Prof. E. Ertekin, Prof. A. M. van der Zande, Prof. P. Y. Huang
Materials Research Laboratory
University of Illinois at Urbana-Champaign
Urbana, IL 61801, USA

DOI: 10.1002/adma.202007269

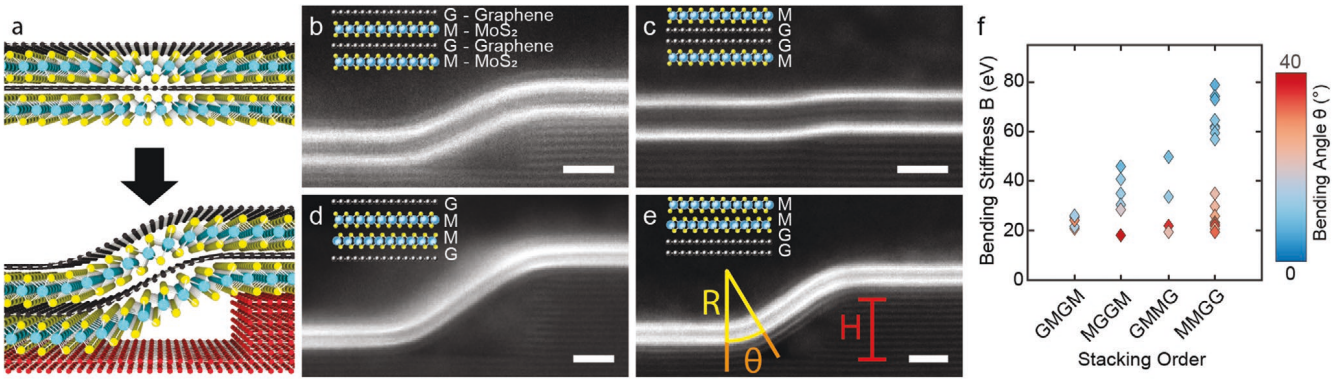

Figure 1. Bending of four-layer 2D heterostructures composed of two graphene (G) and two MoS_2 (M) layers. a) Schematic of a heterostructure draped over an atomically sharp step of h-BN. b–e) Cross-sectional ADF-STEM images of four different 2D heterostructures (GMGM, MGGM, GMMG, and MMGG) with identical composition but different stacking orders. We measure the bending profile of each heterostructure through geometric parameters: the radius of curvature (R), bending angle (θ), and step height (H), as shown in Figure 1e. Scale bars are 2 nm. f) Plot of bending stiffness for each heterostructure, colored by bending angle. MGGM, GMMG, and MMGG show a strong bending angle dependence in bending stiffness. In contrast, GMGM shows no bending angle dependence. At low bending angles, the measured bending stiffness is higher for structures with more aligned interfaces (those containing MM or GG). At high bending angles, the bending stiffnesses of all four structures converge to approximately 20–25 eV.

demonstrate methods to vary the bending stiffness by several hundred percent. A particularly interesting limit occurs when each atomic layer is separated by misaligned hetero- or twisted interfaces. We show that in such systems, the bending stiffness of the overall structures scales as the linear sum of the bending stiffness of each individual layer. This limit represents the theoretical lower limit of bending stiffness of 2D heterostructures. Such control will be instrumental in the design of emerging classes of devices that take advantage of the low intrinsic bending stiffness of atomically thin films to create highly deformable devices, including nanoscale origami or kirigami machines[20–23] and flexible 2D electronics.[24–29]

3. Results and Discussion

In **Figure 1**, we demonstrate that interfacial engineering offers profound control over the bending stiffness of 2D multilayers and heterostructures. We study the bending of four-layer 2D heterostructures formed from stacks of graphene and MoS_2 draped over discrete atomic steps in hexagonal boron nitride (h-BN), shown graphically in Figure 1a. By using h-BN steps of different heights, we vary the degree of deformation of the laminated structure. This configuration allows us to apply controlled out-of-plane deformations to 2D materials and measure the resulting bends using aberration-corrected scanning transmission electron microscopy (STEM). Figure 1b–e shows cross-sectional STEM images of four-layer heterostructures on h-BN steps in different stacking orders: b) graphene/MoS_2/graphene/MoS_2 (GMGM), c) MoS_2/Bernal-stacked bilayer graphene/MoS_2 (MGGM), d) graphene/2H-stacked bilayer MoS_2/graphene (GMMG), and e) 2H-stacked bilayer MoS_2/Bernal-stacked bilayer graphene (MMGG). We categorize inverted stacking orders (e.g., GMGM vs. MGMG, or MMGG vs. GGMM) together in our figures. Because each heterostructure is composed of the same constituent layers, any differences in bending properties must result from the differences in their interfacial interactions.

To fabricate these structures, we use dry pickup and transfer methods[30,31] to sequentially pick up monolayer or bilayer graphene and MoS_2 (see Figure S1, Supporting Information). All of the bilayer components in these structures are obtained via mechanical exfoliation from bulk crystals and are Bernal-stacked for bilayer graphene and 2H-stacked for MoS_2.[32,33] These materials are of similar quality to those used in many 2D heterostructure friction experiments[34–36]; due to their low defect concentration, we do not expect defects to contribute a measurable effect to our bending measurements. Next, we transfer these heterostructures onto atomically sharp h-BN steps and anneal the samples at 350 °C for 10 h. We use Raman spectroscopy and atomic force microscopy (AFM) to confirm the cleanliness and uniformity of the heterostructures (see Figures S2 and S3, Supporting Information), and then we prepare cross-sectional TEM samples using standard focused ion beam lift-out procedures.

As we have previously shown, cross-sectional STEM imaging offers a powerful platform for measuring the bending stiffness of 2D materials.[18] First, we measure the bending profiles of the heterostructures in each STEM image, specifically the radius of curvature R, bending angle θ, and h-BN step height H as shown in Figure 1e. Throughout this paper, we define the bending angle as the angle subtending the two lines perpendicular to the straight sections on either side of the bend. By assuming the structure is in thermodynamic equilibrium, we then apply a simple energetic model in which the conformation is governed by a competition between adhesion and bending (see Section 1.1 in the Supporting Information for derivation). We calculate the bending stiffness from the geometric parameters from each STEM image, using the following equation:[18]

$$B = R\Gamma\left(\frac{H-2R(1-\cos\theta)}{\sin^2\theta}\right) \quad (1)$$

Here, B is the bending stiffness or flexural rigidity of the material stack, similar to the continuum bending stiffness of isotropic materials EI, rather than the stiffness of the entire

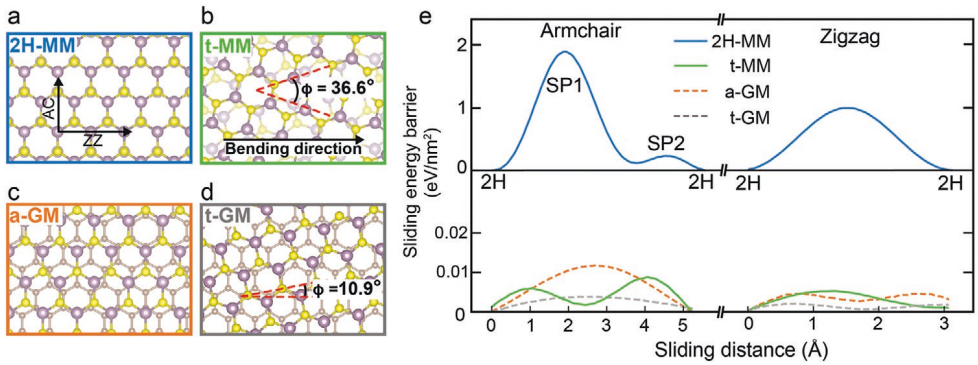

Figure 2. DFT calculations for the interlayer sliding energy barrier of aligned, twisted, and heterointerfaces in 2D materials. 1.1 Top view of DFT simulated atomic structure of: a) 2H-stacked bilayer MoS_2 (2H-MM), b) twisted bilayer MoS_2 (t-MM), c) non-twisted graphene–MoS_2 (a-GM), and d) twisted graphene–MoS_2 (t-GM). The red dotted lines in (b) and (d) indicate the twist angle ϕ between the top and bottom layers. e) Plot of DFT simulated sliding energy barriers of bilayer MoS_2 (solid line) and graphene–MoS_2 (dashed line) versus the sliding distance along two different sliding directions (armchair and zigzag). For each structure, the sliding direction is defined in reference to the bottom layer. SP1 and SP2 indicate barrier heights at the saddle points. The line colors represent different structures: 2H-MM (blue), t-MM (green), a-GM (orange), and t-GM (grey). The barrier heights for the aligned structure 2H-MM are two to three orders of magnitude larger than for the three misaligned interfaces (t-MM, a-GM, and t-GM).

structure. Γ is the interfacial adhesion energy between the bottom layer of the stack and the h-BN substrate (126 mJ m^{-2} for graphene/h-BN and 136 mJ m^{-2} for MoS_2/h-BN).[37,38] For each heterostructure, we image and measure several bending profiles—35 different steps in total (see Figures S4–S7, Supporting Information). In calculating *B*, the two biggest sources of error stem from the measurement of the geometric parameters and uncertainty in the adhesion energy Γ (further discussion in Section 1.1 in the Supporting Information). Despite these potential sources of error, we have previously shown that our methods provide highly accurate and precise measurements of *B* for 2D materials.[18]

Figure 1f shows the extracted bending stiffness of each four-layer heterostructure (see Figure S8, Supporting Information for error bars, which are left off here for clarity). Notably, while the minimum values of *B* for all four structures cluster around 20 eV, the range of *B* increases with the number of aligned interfaces in the stack. The bending stiffness of MMGG, where MoS_2 and graphene occur as aligned bilayers, shows the widest spread of 20–80 eV. In contrast, the bending stiffnesses of GMGM, where the graphene and MoS_2 layers alternate, are tightly clustered between 20–26 eV. Another difference emerges when we examine the dependence of bending stiffness on bending angle, indicated by the color coding in Figure 1f. The bending stiffnesses are inversely correlated with bending angle for the three structures that contain aligned interfaces (MGGM, GMMG, and MMGG), while we observe no bending angle dependence for GMGM. These data demonstrate the key role of interfaces in tuning the bending stiffness of 2D heterostructures—they determine both the quantitative values and the bending angle-dependent trends in *B*.

In **Figure 2**, we use density functional theory (DFT)[39,40] to simulate the interfacial interactions present in a 2H-stacked bilayer MoS_2 (2H-MM), twisted bilayer MoS_2 (t-MM), and graphene–MoS_2 (GM) heterostructure (see Section 1.2 and Figure S9, Supporting Information for simulation details). These bilayers represent the different interface types in 2D multilayers: an aligned interface between like materials (2H-MM) and misaligned interfaces from either interlayer twist (t-MM) or lattice mismatch (GM). We use the term "misaligned" to encompass both commensurate and incommensurate twisted and heterointerfaces because we find these structures behave similarly. Figure 2a–d shows top-down schematics for 2H-MM, t-MM (for twist angle ϕ = 36.6°) and GM (for ϕ = 0° and ϕ = 10.9°). Figure 2e shows the simulated sliding energy landscape for each bilayer, representing the energy required to displace one layer relative to the other along each of two directions: armchair (AC) $\langle\bar{1}100\rangle$ and zigzag (ZZ) $\langle\bar{2}110\rangle$. In each structure, the sliding direction is defined in reference to the bottom layer. 2D multilayers bend primarily via interlayer shear and slip,[18] where each atomic layer slides to accommodate the geometric arc length differences. In this context, the interfacial sliding energy barrier contributes to the effective bending stiffness of the 2D stack because it resists slip. The sliding energy barrier height for 2H-MM is 1–2 eV nm^{-2}, two orders of magnitude larger than those for t-MM and GM (0.01–0.02 eV nm^{-2}), consistent with the Frenkel–Kontorova model, which describes the origin of reduced interlayer friction in 2D multilayers at heterointerfaces and twisted interfaces.[17,34,35,41,42] These plots also show that the interlayer friction is strongly dependent on the sliding direction and crystallographic bending direction for aligned bilayer MoS_2,[42,43] but not for twisted interfaces and heterointerfaces. We obtain similar results for the 1T phase of MoS_2 (see Figure S19, Supporting Information). By directly comparing 2H-MM, t-MM, and GM, our studies show that either introducing twist or heterointerfaces reduces the interlayer sliding energy barrier, and should therefore reduce the bending stiffness of 2D stacks.

In **Figure 3**, we examine how the differing interlayer interactions of twisted, aligned, and heterointerfaces affect the bending properties of 2D bilayers t-MM, 2H-MM, and GM. Figure 3a–d shows cross-sectional STEM images of monolayer MoS_2 (M), t-MM, 2H-MM, and GM bent over h-BN steps. Figure 3e,f plot the experimental and DFT calculations of *B* for each structure (see Figure S10–S14, Supporting Information for raw experimental data and error bars). In the DFT simulations, the bending stiffness is evaluated by measuring the energy required to deform the bilayers

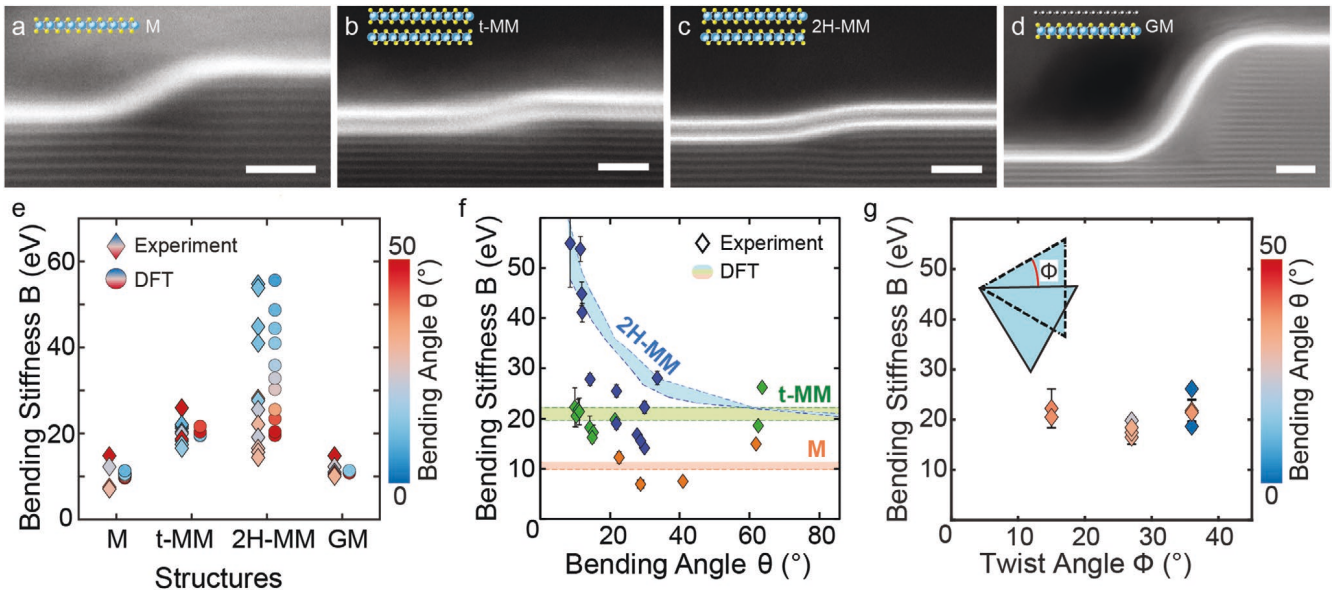

Figure 3. Experimental and DFT bending measurements of aligned, twisted, and heterostructure bilayers. a–d) Cross-sectional ADF-STEM images of: a) monolayer MoS_2 (M), b) twisted bilayer MoS_2 (t-MM), c) 2H-stacked bilayer MoS_2 (2H-MM), and d) a graphene–MoS_2 heterostructure (GM). Scale bars are 2 nm. e) Plot of experimental (diamonds) and DFT (circles) values of bending stiffness for each structure, colored by bending angle. 2H-MM, the only structure with an aligned interface, shows the widest spread in bending stiffness spanning 14–55 eV with a strong bending angle dependence. f) Bending stiffness versus bending angle for 2H-MM, t-MM, and M. The error bars represent one standard error propagated from measurement precision. The upper and lower limits of the shaded regions indicate DFT predictions for bending along the zigzag and armchair directions. 2H-MM converges with t-MM at high bending angles. g) Impact of twist angle on bending stiffness for twisted bilayer MoS_2. We observe no impact of t-MM bending stiffness on twist angle or bending angle.

into rippled structures (simulation details in Section 1.3 and Figures S15 and S16, Supporting Information).[18,44] In Figure 3e, we see strong agreement between experimental and DFT values. For monolayer MoS_2, we obtain a mean B of 10.1 ± 0.3 eV from DFT and 10.5 ± 3.8 eV from experiment, consistent with literature values.[45,46] For the bilayer structures, Figure 3e,f show a strong bending angle-dependent bending stiffness for the aligned interface in 2H-MM, but not for the twisted and heterointerfaces in t-MM and GM. Figure 3g examines the bending stiffness of twisted bilayer MoS_2 as a function of interlayer twist angle (also see Figure S17, Supporting Information). We find that the bending stiffness of t-MM does not exhibit a measurable dependence on the interlayer twist angle.

We can understand the data in Figure 3 by breaking down the bending stiffness of 2D multilayers and heterostructures into contributions from each constituent monolayer and interface. For the misaligned or twisted structures, the experimental measurements yield $B_{t\text{-MM}}$ = 20.3 ± 2.8 eV and B_{GM} = 11.8 ± 1.9 eV, very close to the sum of bending stiffness of their individual component layers. These data indicate that misaligned interfaces either from heterointerfaces or nonzero twist angles provide a negligible interfacial contribution to the bending stiffness. We expect these results to hold for any misaligned interface where there is not significant lattice reconstruction, which may alter the interlayer friction.[15,47–49]

In contrast, the interfacial contribution to the bending stiffness for aligned multilayers is comparable to or even larger than the intrinsic bending stiffness of the individual layers across a wide range of bending angles. The bending stiffness of bilayer 2H-MM gradually decreases from 60 to 20 eV with increasing bending angle, converging to that of t-MM for bending angles above 30–60°. This trend echoes what we previously observed in aligned few-layer graphene, and is a result of the reduction of the interlayer atomic registry and corresponding reduction in the interlayer friction as the material is bent.[18] From this trend, we conclude that the additional bending stiffness at low bending angles arises from interfacial interactions. For example, we measured a 2H-MM structure at a bending angle of 10°, finding an effective bending stiffness of 55 eV, reflecting a contribution of 21 eV from the intrinsic bending stiffness of the two MoS_2 layers and 34 eV from the interfacial interactions.

Using these insights, we develop a model to predict and design the bending stiffness of arbitrary 2D heterostructures:

$$B = \sum_{i}^{N} B_{\mathrm{ml},i} + \sum_{j}^{N-1} a \cdot S_j(\theta) \cdot (R_j \cdot \theta)^2 \quad (2)$$

where N is the total number of layers, $B_{\mathrm{ml},\,i}$ is the monolayer bending stiffness of the ith layer, a is a geometric factor that describes the boundary conditions (details in Section 1.4 in the Supporting Information), and θ is the bending angle. R_j and $S_j(\theta)$ are respectively the radius of curvature and interfacial shear energy at the jth interface. While we focus on graphene and MoS_2 in this work, we expect our model to be generalizable across van der Waals bonded materials. This model is an atomistic version of continuum anisotropic Timoshenko and laminated beam theories,[50–53] where the material and interfacial values arise from discrete and nonlinear atomic scale interactions rather than continuum linear elastic constants or the

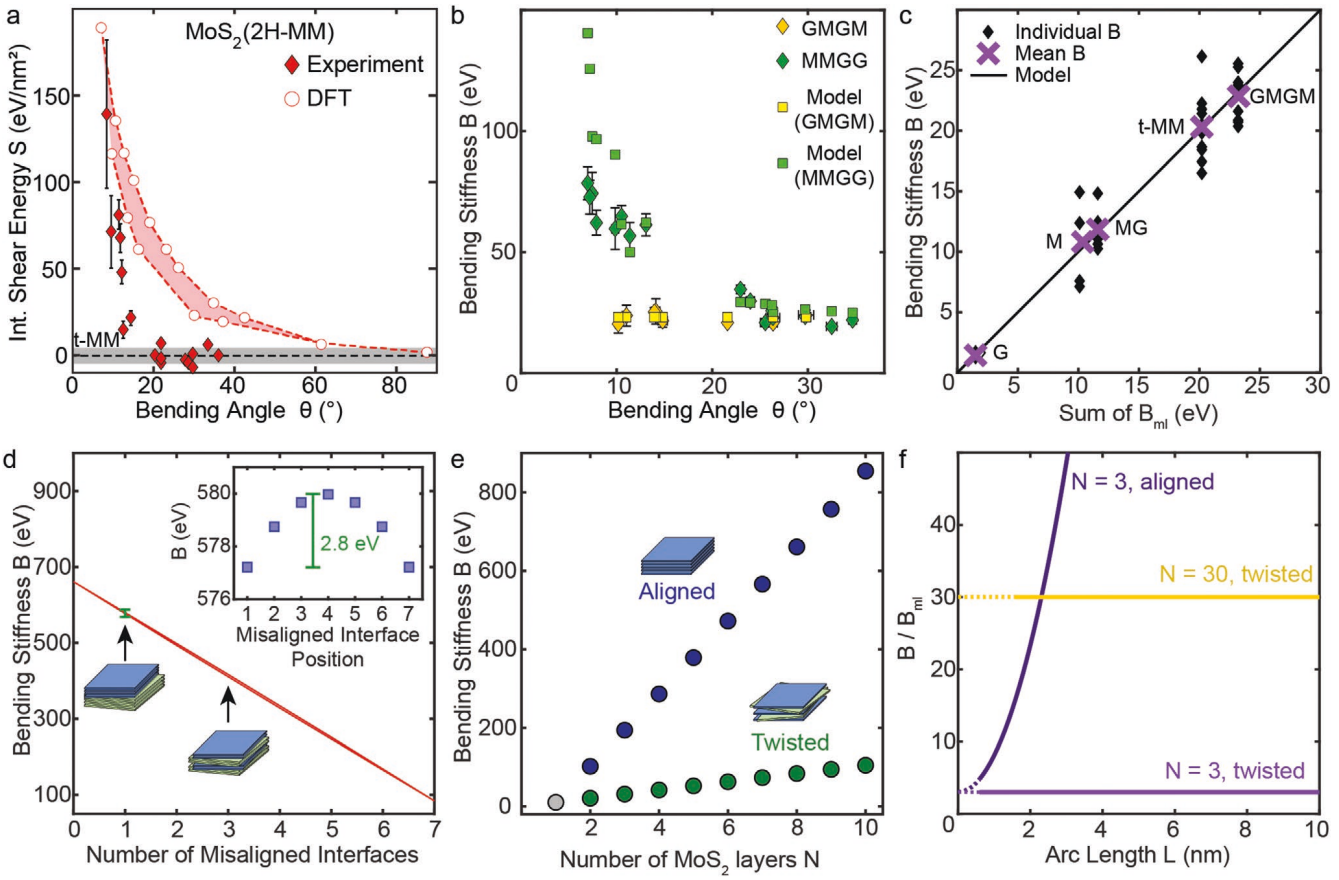

Figure 4. Bending model and design rules for deformable 2D multilayers and heterostructures. a) Interfacial shear energy $S(\theta)$ for 2H-MM, calculated from experiment (filled diamonds) and DFT (empty circles). The red shading indicates the spread in DFT predictions between bending along the zigzag and armchair directions. The gray dashed line and shading indicates mean and spread in experimentally derived S of *t*-MM propagated from measurement error. b) Bending stiffness of MMGG (green) and GMGM (yellow). The diamonds indicate experimental values from STEM images, whereas the squares indicate predicted values from the model. The error bars represent one standard error propagated from measurement precision. c) Experimental measurements and model predictions of bending stiffness for structures without aligned interfaces: monolayer graphene, monolayer MoS_2, *t*-MM, GM, and GMGM. For each structure, the mean experimental B (purple crosses) is within 0.4 eV of the model predictions(black line). d) Bending stiffness versus number of misaligned interfaces for 8-layer MoS_2. For (d–e), a symmetric S-shape is assumed with $\theta = 10°$ and radius of curvature $R = 10$ nm at the neutral axis. For this structure, B tunes by more than 600% with the number of misaligned interfaces. Inset in (d): Dependence of bending stiffness on position of a misaligned interface for a structure containing one misaligned interface. e) Bending stiffness versus thickness for aligned and twisted MoS_2 multilayers. The slope of B with thickness for misaligned stacks is equal to the monolayer bending stiffness. f) Bending stiffness versus arc length for aligned and twisted multilayer MoS_2 with $\theta = 10°$. The bending stiffness of aligned stacks scales quadratically with the system size but is constant for misaligned stacks. The dashed lines indicate when the prediction becomes nonphysical at small bend sizes where R approaches the thickness of the 2D stack.

Amonton–Coulomb description of friction. A key term in this equation is the interfacial shear energy $S_j(\theta)$, which represents the contribution of an interface to the total bending energy. $S(\theta)$ in aligned interfaces is distinct from the continuum shear modulus G because it is not a constant, but instead depends on bending angle. Because S is dependent on the atomic arrangements at each interface, it can be directly manipulated via interfacial engineering.

Figure 4a compares the experimentally derived and computationally predicted values of $S(\theta)$ for aligned 2H-MM and misaligned t-MM (see Section 1.5 and Figure S18, Supporting Information for $S(\theta)$ for graphene). Red shading indicates the difference in DFT predictions for bending along the zigzag and armchair directions; this spread exists because, for aligned multilayers, the bending stiffness is dependent on the bending direction with respect to the crystal lattice.[18] From experiment, we observe $S_{2H\text{-}MM}$ and $S_{BS\text{-}GG}$ (for Bernal-stacked bilayer graphene) up to 140 and 95 eV nm^{-2}, respectively; these large values indicate that the interfacial interactions $S(\theta)$ dominate at low bending angles. In contrast, we measured $S_{t\text{-}MM} = -0.5 \pm 4.7$ eV nm^{-2} and $S_{GM} = -0.2 \pm 1.4$ eV nm^{-2}. These values are zero to within our measurement error, confirming that twisted and heterointerfaces are nearly frictionless and thus do not contribute to the bending stiffness.

In Figure 4b,c, we show that our model can quantitatively predict the bending stiffness of arbitrarily complex 2D heterostructures, including those which are too large to simulate directly using first-principles calculations. Figure 4b plots the bending stiffness versus bending angle for four-layer heterostructures GMGM and MMGG measured experimentally (diamonds) and predicted by our model (squares). For our prediction using Equation (2), B_{ml} comes from DFT, while

R, θ, and S are derived from experiment. Overall, we obtain strong agreement between experiment and the model for both structures. For GMGM (yellow), the model predicts a constant B = 23.0 eV across all bending angles, as compared to 22.8 ± 2.1 eV from experiment. For MMGG (green), our model yields B that are accurate to within our experimental error for each structure; mismatch between the model predictions and experiment primarily arises from uncertainty in $S(\theta)$ because the bending direction is unknown and different between each sample.

For structures where each individual layer is separated by twisted or heterointerfaces, S approaches zero and the bending stiffness (Equation (2)) simplifies to:

$$B = \sum_{i}^{N} B_{ml,i} \tag{3}$$

Figure 4c plots the experimentally measured bending stiffness of GM, t-MM, and GMGM—all structures with only misaligned interfaces—against the sum of their monolayer bending stiffness components B_{ml} predicted from DFT. We also include values for monolayer graphene (G),[18] and monolayer MoS_2 (M) for reference. While there is a spread in the individual measurements of B (black diamonds), we find that the mean experimental B for each structure (purple crosses) can be predicted to within 0.4 eV of our model prediction (black line). This behavior may be understood in the context of continuum mechanics laminated beam theory, where the bending stiffness of a stack of frictionless beams is equal to the sum of bending stiffness of each beam, leading to a bending stiffness that scales linearly with the number of layers and represents the theoretical lower limit of bending stiffness for a 2D multilayer.

In Figure 4d–f, we utilize our bending model to establish design rules to control the bending stiffness of 2D heterostructures. First, because S approaches zero for misaligned interfaces, incorporating twisted and heterointerfaces will decrease B. This principle is illustrated in Figure 4d, where we apply the model to predict how the bending stiffness should vary for 8-layer MoS_2 as a function of the number of twisted (i.e., misaligned) interfaces. For this prediction, we assume a symmetric S-shaped curve with a constant bending angle $\theta = 10°$ ($S_{\mathrm{2H-MM}}(\theta)$ = 80 eV nm^{-2}) and radius of curvature R = 10 nm at the neutral axis. In a fixed geometry, the bending stiffness decreases roughly linearly with the number of heterointerfaces. B is also weakly dependent on the location of the twisted interface (see inset, Figure 4d and width of red line in 4d). For a fixed number of twisted interfaces, the B is highest when the twisted interfaces are closest to the center of the 2D multilayer. The symmetric position dependence is a result of the symmetric S-shaped curve used, so interface 1 is equivalent to interface N-1.

Figure 4e,f shows that interfacial engineering becomes more important when the overall thickness and size of the 2D multilayers increase. Figure 4e plots the bending stiffness as a function of thickness for aligned (2H-stacked) and misaligned (twisted) multilayer MoS_2, under the same fixed geometry as in Figure 4d. Figure 4f plots the bending stiffness of aligned or misaligned multilayer MoS_2 of different thicknesses as a function of arc length L, which represents the length of the sample that is bent to a constant curvature. In both cases, the relative contribution from the interface compared with the constituent monolayers increases drastically as a function of thickness or bend size. In the misaligned multilayers, the bending stiffness is a linear sum of the stiffness of each layer, and it is independent of the size of the bend. The dependence of B with N and L for the aligned structure is more complex. For nonzero S, the interfacial contribution to the bending stiffness increases quadratically with the system size and linearly with the number of interfaces; these scaling laws are consistent with the predictions of Timoshenko beam theory for anisotropic materials under large deformations. Importantly, the different scaling properties between aligned and misaligned structures make it so that their stiffnesses diverge rapidly as the size and thickness increase. In the limit of device-scale 2D structures, which typically contain a dozen or more layers and large bends tens or hundreds of nanometers across, our model indicates that misaligned structures can be made orders of magnitude more deformable than aligned 2D materials or conventional thin films.

These observations have important implications for the design of 2D heterostructure devices. First, our results demonstrate that the bending stiffness can be tuned over a large range by manipulating the number—and to a lesser extent, the location—of misaligned interfaces in 2D stacks. Second, interfacial engineering makes it possible to obtain low B structures, even in devices with a large number of layers. Whereas the bending stiffness increases rapidly with thickness for conventional thin films, Figure 4 shows that incorporating misaligned interfaces makes it possible to maintain extremely low B, even in 2D multilayers. The impact of interfacial engineering is so significant that, for example, Figure 4f shows that it is possible to fabricate twisted 30-layer MoS_2 that is even more deformable than aligned trilayer MoS_2. Importantly, in structures where each layer is separated by twisted or heterointerfaces, the bending stiffness reaches a minimum and becomes independent of bending angle and system size for nanoscale to microscale curvatures. This theoretical lower limit, where the B is equal to the sum of its constituent B_{ml}, is particularly powerful because 2D monolayers have exceptionally low intrinsic bending stiffness—in the range of 1.4–20 eV, or 60–800 kT at room temperature, on the same order as lipid bilayers.

4. Conclusion

Together, our results demonstrate that interfacial engineering provides a profound opportunity to manipulate and design deformable 2D electronics. First, our work shows that 2D heterostructure devices, a diverse class of 2D electronics, are intrinsically well-suited to deformable electronics. Second, our work provides a roadmap to design 2D multilayers to maximize their out-of-plane deformability by incorporating twisted or heterointerfaces. Because the thickest component of 2D nanoelectronics like transistors is often a h-BN dielectric, such modifications could be made to tune the bending stiffness of 2D devices with minimal impact on their electronic properties. For example, one could design a highly deformable transistor in which each layer—including the h-BN dielectric, MoS_2 active layer,

and graphene gate and contacts—is separated by a twisted or heterointerface. Even in nominally flat 2D electronics, fabrication methods for high-electrical-mobility devices often include local gates or contacts, which produce bent 2D layers.[54,55] In this context, our work can also inform the design of more complex 3D architectures for 2D electronics, including conformal 2D contacts or highly curved 3D circuits. Finally, these design principles will be important for an emerging generation of reconfigurable 2D devices, including folded, curved, and crumpled nanostructures, where they may enable flexible, stretchable, or conformal circuitry that are orders of magnitude more deformable than conventional electronics.

5. Experimental Section

Fabrication of van der Waals Heterostructures: To fabricate graphene–MoS_2 heterostructures, established hot pick-up techniques were utilized to produce clean van der Waals interfaces between graphene and MoS_2 heterostructures.[18,31] First, graphene and MoS_2 were exfoliated onto a SiO_2 (285 nm)/Si substrate with the scotch tape method. To pick up the monolayer flakes, a transparent sacrificial transfer substrate was fabricated. A polydimethylsiloxane (PDMS) droplet was deposited on a glass slide. After curing, the PDMS droplet was covered with a polycarbonate (PC) film and annealed for 10 min to achieve good conformation. The pickup and transfer procedures were accomplished by inserting the target substrates and sacrificial transfer substrate into an aligned transfer station in a nitrogen glovebox. The monolayer or bilayer flakes were picked up by contacting the PC-coated PDMS lens on the designated flake, and increasing the temperature to 90 °C. This process was then repeated to pick up other 2D flakes to form a multilayer stack on the PC-coated PDMS lens. Once the pick up process was done, the multilayer stack was transferred onto terraced hexagonal boron nitride (h-BN), which was exfoliated on the SiO_2 (285 nm)/Si substrate. Once the multilayer stack was fully contacted with terraced h-BN, the substrate temperature was increased to 180 °C to melt PC films to release from the PDMS. After the final transfer, the sample was annealed under high vacuum at 350 °C for 14 h.

To fabricate twisted bilayer MoS_2 with measurable interlayer twist angle,[7] first monolayer single crystals of MoS_2 were synthesized via solid precursor chemical vapor deposition.[56] Monolayer MoS_2 triangles were grown by placing molybdenum trioxide and sulfur solid precursors on top of a SiO_2 (285 nm)/Si substrate and heated to 675 °C for 5 min in an argon environment. The monolayer MoS_2 on the SiO_2 (285 nm)/Si substrate was spin-coated with 5% PC dissolved in chloroform and was attached to the PDMS stamp. The entire structure was then dipped in a KOH solution to detach the SiO_2/Si substrate, leaving the monolayer on the stamp. Next, the monolayer MoS_2 flakes on the PC films were transferred onto another MoS_2 monolayer flake using aligned transfer techniques described above.

TEM Sample Preparation: A protective layer of amorphous carbon that was 5–30 nm thick, was thermally evaporated on top of the 2D heterostructures. Then, cross-sectional STEM samples were fabricated using standard focused ion beam (FIB) lift-out procedures in a FEI Helios 600i Dual Beam FIB-SEM. Final milling was done at 2 kV to reduce sample damage, using a cryo-can to minimize redeposition.

Aberration-corrected STEM Imaging: The cross-sectional samples were imaged in a Thermo Fisher Scientific Themis Z aberration-corrected STEM. The STEM was operated at 80 kV, below the knock-on damage thresholds of graphene and h-BN, and close to the knock-on damage threshold for MoS_2. A convergence angle of 25.2 mrad was used.

Density Functional Theory Calculations: The Vienna Ab initio Simulation Package (VASP)[57] with the projector augmented wave pseudopotentials[58] was used to conduct density functional theory simulations.[39,40] A van der Waals density functional, vdW-DF2,[59] was used to incorporate van der Waals adhesion between different 2D materials. An energy cutoff of the plane wave basis is 350 eV, with a total energy conversion criteria of 10^{-4} eV. 30 Å of vacuum was included to avoid self-interaction of the 2D material membranes in the periodic boundary conditions. In Figure 2, the sliding barrier of the bilayers was calculated from the difference in the total energy of each configuration (aligned, twisted, heterostructure) when one layer slides with respect to the other layer compared with the lowest energy position for each configuration. The displacement of each step was 0.1 Å. In order to calculate the bending energy through simulation, bending was introduced in the 2D heterostructure by reducing the size of supercell in a given direction along the basal plane. To induce out of plane buckling, a small geometric perturbation was introduced to the initial configuration. To find the ground state geometry, the geometry were allowed to relax until the forces on each atom were below 0.04 eV $Å^{-1}$. The bending energy was then estimated by subtracting the energy of the flat, uncompressed structure. The derivation of bending stiffness from local curvature in the simulation is discussed in Section 1.3 in the Supporting Information.

Supporting Information

Supporting Information is available from the Wiley Online Library or from the author.

Acknowledgements

J.Y. and E.H. contributed equally to this work. This work was supported by NSF-MRSEC award number DMR-1720633. The work was carried out in part in the Micro and Nano Technology Laboratory and the Materials Research Laboratory Central Facilities at the University of Illinois, where electron microscopy support was provided by J. Mabon, C. Chen, and H. Zhou. The authors acknowledge the use of facilities and instrumentation supported by the NSF through the University of Illinois Materials Research Science and Engineering Center award number DMR-1720633. Computational resources were provided by the Illinois Campus Computing Cluster. K.W. and T.T. acknowledge support from the Elemental Strategy Initiative conducted by the MEXT, Japan, award number JPMXP0112101001, JSPS KAKENHI award number JP20H00354 and the JST CREST award number JPMJCR15F3. The authors acknowledge helpful discussions with Jangyup Son, Emil Annevelink, Blanka Janicek, and Sunphil Kim.

Conflict of Interest

The authors declare no conflict of interest.

Keywords

2D heterostructures, bending mechanics, deformable materials, electron microscopy, interfacial engineering

Received: October 23, 2020
Revised: November 30, 2020
Published online: January 25, 2021

[1] A. K. Geim, I. V. Grigorieva, *Nature* **2013**, *499*, 419.
[2] K. S. Novoselov, A. Mishchenko, A. Carvalho, A. H. Castro Neto, *Science* **2016**, *353*, 6298.
[3] Y. Cao, V. Fatemi, S. Fang, K. Watanabe, T. Taniguchi, E. Kaxiras, P. Jarillo-Herrero, *Nature* **2018**, *556*, 43.

[4] R. Ribeiro-Palau, C. Zhang, K. Watanabe, T. Taniguchi, J. Hone, C. R. Dean, *Science* **2018**, *361*, 690.
[5] N. R. Finney, M. Yankowitz, L. Muraleetharan, K. Watanabe, T. Taniguchi, C. R. Dean, J. Hone, *Nat. Nanotechnol.* **2019**, *14*, 1029.
[6] S. Shallcross, S. Sharma, E. Kandelaki, O. A. Pankratov, *Phys. Rev. B: Condens. Matter Mater. Phys.* **2010**, *81*, 165105.
[7] A. M. van der Zande, J. Kunstmann, A. Chernikov, D. A. Chenet, Y. You, X. Zhang, P. Y. Huang, T. C. Berkelbach, L. Wang, F. Zhang, M. S. Hybertsen, D. A. Muller, D. R. Reichman, T. F. Heinz, J. C. Hone, *Nano Lett.* **2014**, *14*, 3869.
[8] S. Huang, X. Ling, L. Liang, J. Kong, H. Terrones, V. Meunier, M. S. Dresselhaus, *Nano Lett.* **2014**, *14*, 5500.
[9] V. Perebeinos, J. Tersoff, P. Avouris, *Phys. Rev. Lett.* **2012**, *109*, 236604.
[10] T. Chari, R. Ribeiro-Palau, C. R. Dean, K. Shepard, *Nano Lett.* **2016**, *16*, 4477.
[11] O. Hod, E. Meyer, Q. Zheng, M. Urbakh, *Nature* **2018**, *563*, 485.
[12] M. Dienwiebel, G. S. Verhoeven, N. Pradeep, J. W. M. Frenken, J. A. Heimberg, H. W. Zandbergen, *Phys. Rev. Lett.* **2004**, *92*, 126101.
[13] Z. Liu, J. Yang, F. Grey, J. Z. Liu, Y. Liu, Y. Wang, Y. Yang, Y. Cheng, Q. Zheng, *Phys. Rev. Lett.* **2012**, *108*, 205503.
[14] X. Feng, S. Kwon, J. Y. Park, M. Salmeron, *ACS Nano* **2013**, *7*, 1718.
[15] J. S. Alden, A. W. Tsen, P. Y. Huang, R. Hovden, L. Brown, J. Park, D. a. Muller, P. L. McEuen, *Proc. Natl. Acad. Sci. USA* **2013**, *110*, 11256.
[16] L. Jiang, Z. Shi, B. Zeng, S. Wang, J.-H. Kang, T. Joshi, C. Jin, L. Ju, J. Kim, T. Lyu, Y.-R. Shen, M. Crommie, H.-J. Gao, F. Wang, *Nat. Mater.* **2016**, *15*, 840.
[17] S. Kim, J. Yu, A. M. van der Zande, *Nano Lett.* **2018**, *18*, 6686.
[18] E. Han, J. Yu, E. Annevelink, J. Son, D. A. Kang, K. Watanabe, T. Taniguchi, E. Ertekin, P. Y. Huang, A. M. van der Zande, *Nat. Mater.* **2020**, *19*, 305.
[19] G. Wang, Z. Dai, J. Xiao, S. Feng, C. Weng, L. Liu, Z. Xu, R. Huang, Z. Zhang, *Phys. Rev. Lett.* **2019**, *123*, 116101.
[20] M. K. Blees, A. W. Barnard, P. A. Rose, S. P. Roberts, K. L. McGill, P. Y. Huang, A. R. Ruyack, J. W. Kevek, B. Kobrin, D. A. Muller, P. L. McEuen, *Nature* **2015**, *524*, 204.
[21] M. Z. Miskin, K. J. Dorsey, B. Bircan, Y. Han, D. A. Muller, P. L. McEuen, I. Cohen, *Proc. Natl. Acad. Sci. USA* **2018**, *115*, 466.
[22] M. F. Reynolds, K. L. McGill, M. A. Wang, H. Gao, F. Mujid, K. Kang, J. Park, M. Z. Miskin, I. Cohen, P. L. McEuen, *Nano Lett.* **2019**, *19*, 6221.
[23] W. Xu, T. Li, Z. Qin, Q. Huang, H. Gao, K. Kang, J. Park, M. J. Buehler, J. B. Khurgin, D. H. Gracias, *Nano Lett.* **2019**, *19*, 7941.
[24] G. H. Lee, Y. J. Yu, X. Cui, N. Petrone, C. H. Lee, M. S. Choi, D. Y. Lee, C. Lee, W. J. Yoo, K. Watanabe, T. Taniguchi, C. Nuckolls, P. Kim, J. Hone, *ACS Nano* **2013**, *7*, 7931.
[25] D. Akinwande, N. Petrone, J. Hone, *Nat. Commun.* **2014**, *5*, 5678.
[26] J. Zang, S. Ryu, N. Pugno, Q. Wang, Q. Tu, M. J. Buehler, X. Zhao, *Nat. Mater.* **2013**, *12*, 321.
[27] S. Deng, V. Berry, *Mater. Today* **2016**, *19*, 197.
[28] P. Kang, M. C. Wang, P. M. Knapp, S. Nam, *Adv. Mater.* **2016**, *28*, 4639.
[29] J. Yu, S. Kim, E. Ertekin, A. M. van der Zande, *ACS Appl. Mater. Interfaces* **2020**, *12*, 10801.
[30] J. Son, J. Kwon, S. P. Kim, Y. Lv, J. Yu, J.-Y. Y. Lee, H. Ryu, K. Watanabe, T. Taniguchi, R. Garrido-Menacho, N. Mason, E. Ertekin, P. Y. Huang, G. H. Lee, A. M. van der Zande, *Nat. Commun.* **2018**, *9*, 3988.
[31] F. Pizzocchero, L. Gammelgaard, B. S. Jessen, J. M. Caridad, L. Wang, J. Hone, P. Bøggild, T. J. Booth, *Nat. Commun.* **2016**, *7*, 11894.
[32] Y. Yang, Y.-C. Zou, C. R. Woods, Y. Shi, J. Yin, S. Xu, S. Ozdemir, T. Taniguchi, K. Watanabe, A. K. Geim, K. S. Novoselov, S. J. Haigh, A. Mishchenko, *Nano Lett.* **2019**, *19*, 8526.
[33] J. Shi, P. Yu, F. Liu, P. He, R. Wang, L. Qin, J. Zhou, X. Li, J. Zhou, X. Sui, S. Zhang, Y. Zhang, Q. Zhang, T. C. Sum, X. Qiu, Z. Liu, X. Liu, *Adv. Mater.* **2017**, *29*, 1701486.
[34] H. Li, J. Wang, S. Gao, Q. Chen, L. Peng, K. Liu, X. Wei, *Adv. Mater.* **2017**, *29*, 1701474.
[35] L. Wang, J. Luo, X. Zhou, T. Ma, D. Liu, D. Liu, L. Gao, X. Li, J. Zhang, Y. Hu, H. Wang, Y. Dai, J. Luo, *Nanoscale* **2017**, *9*, 10846.
[36] M. R. Vazirisereshk, H. Ye, Z. Ye, A. Otero-de-la Roza, M.-Q. Zhao, Z. Gao, A. T. C. Johnson, E. R. Johnson, R. W. Carpick, A. Martini, *Nano Lett.* **2019**, *19*, 5496.
[37] E. Khestanova, F. Guinea, L. Fumagalli, A. K. Geim, I. V. Grigorieva, *Nat. Commun.* **2016**, *7*, 12587.
[38] D. A. Sanchez, Z. Dai, P. Wang, A. Cantu-Chavez, C. J. Brennan, R. Huang, N. Lu, *Proc. Natl. Acad. Sci. USA* **2018**, *115*, 7884.
[39] P. Hohenberg, W. Kohn, *Phys. Rev.* **1964**, *136*, B864.
[40] W. Kohn, L. J. Sham, *Phys. Rev.* **1965**, *140*, A1133.
[41] Y. Shibuta, J. A. Elliott, *Chem. Phys. Lett.* **2011**, *512*, 146.
[42] B. J. Irving, P. Nicolini, T. Polcar, *Nanoscale* **2017**, *9*, 5597.
[43] V. E. Claerbout, T. Polcar, P. Nicolini, *Comput. Mater. Sci.* **2019**, *163*, 17.
[44] Y. Guo, J. Qiu, W. Guo, *Nanotechnology* **2017**, *28*, 195701.
[45] J. Zhao, Q. Deng, T. H. Ly, G. H. Han, G. Sandeep, M. H. Rümmeli, *Nat. Commun.* **2015**, *6*, 8935.
[46] S. Xiong, G. Cao, *Nanotechnology* **2016**, *27*, 105701.
[47] C. R. Woods, L. Britnell, A. Eckmann, R. S. Ma, J. C. Lu, H. M. Guo, X. Lin, G. L. Yu, Y. Cao, R. V. Gorbachev, A. V. Kretinin, J. Park, L. A. Ponomarenko, M. I. Katsnelson, Y. N. Gornostyrev, K. Watanabe, T. Taniguchi, C. Casiraghi, H.-J. Gao, A. K. Geim, K. S. Novoselov, *Nat. Phys.* **2014**, *10*, 451.
[48] S. S. Sunku, G. X. Ni, B. Y. Jiang, H. Yoo, A. Sternbach, A. S. McLeod, T. Stauber, L. Xiong, T. Taniguchi, K. Watanabe, P. Kim, M. M. Fogler, D. N. Basov, *Science* **2018**, *362*, 1153.
[49] A. Kerelsky, L. J. McGilly, D. M. Kennes, L. Xian, M. Yankowitz, S. Chen, K. Watanabe, T. Taniguchi, J. Hone, C. Dean, A. Rubio, A. N. Pasupathy, *Nature* **2019**, *572*, 95.
[50] L. D. Landau, E. M. Lifshitz, *Theory of Elasticity*, Course of Theoretical Physics, Vol. *7*, Butterworth Heinemann, Oxford, UK **1986**.
[51] M. S. Qatu, *Int. J. Solids Struct.* **1993**, *30*, 2743.
[52] Y. Liu, Z. Xu, Q. Zheng, *J. Mech. Phys. Solids* **2011**, *59*, 1613.
[53] H. Qin, Y. Yan, H. Lui, J. Liu, Y.-W. Zhang, *Extreme Mech. Lett.* **2020**, *39*.
[54] L. Wang, I. Meric, P. Y. Huang, Q. Gao, Y. Gao, H. Tran, T. Taniguchi, K. Watanabe, L. M. Campos, D. A. Muller, J. Guo, P. Kim, J. Hone, K. L. Shepard, C. R. Dean, *Science* **2013**, *342*, 614.
[55] X. Cui, G.-H. Lee, Y. D. Kim, G. Arefe, P. Y. Huang, C.-H. Lee, D. A. Chenet, X. Zhang, L. Wang, F. Ye, F. Pizzocchero, B. S. Jessen, K. Watanabe, T. Taniguchi, D. A. Muller, T. Low, P. Kim, J. Hone, *Nat. Nanotechnol.* **2015**, *10*, 534.
[56] A. M. van der Zande, P. Y. Huang, D. a. Chenet, T. C. Berkelbach, Y. You, G.-H. Lee, T. F. Heinz, D. R. Reichman, D. a. Muller, J. C. Hone, *Nat. Mater.* **2013**, *12*, 554.
[57] G. Kresse, J. Furthmüller, *Comput. Mater. Sci.* **1996**, *6*, 15.
[58] P. E. Blöchl, *Phys. Rev. B* **1994**, *50*, 17953.
[59] J. Klimeš, D. R. Bowler, A. Michaelides, *Phys. Rev. B* **2011**, *83*, 195131.

